White Rose Research Online

eprints@whiterose.ac.uk
https://eprints.whiterose.ac.uk
Universities of Leeds, Sheffield and York

Deposited via The University of Leeds.

White Rose Research Online URL for this paper:
https://eprints.whiterose.ac.uk/id/eprint/137202/

Version: Accepted Version

Article:
Galadzhun, I, Kulmaczewski, R, Cespedes, O et al. (2018) 2,6-Di(pyrazol-1-yl)pyridine-4-carboxylate Esters with Alkyl Chain Substituents, and their Iron(II) Complexes. Inorganic Chemistry, 57 (21). pp. 13047-14012. ISSN: 0020-1669

https://doi.org/10.1021/acs.inorgchem.8b02289

© 2018 American Chemical Society. This document is the Accepted Manuscript version of a Published Work that appeared in final form in Inorganic Chemistry, copyright © American Chemical Society after peer review and technical editing by the publisher. To access the final edited and published work see https://pubs.acs.org/doi/10.1021/acs.inorgchem.8b02289. Uploaded in accordance with the publisher's self-archiving policy.

Reuse
Items deposited in White Rose Research Online are protected by copyright, with all rights reserved unless indicated otherwise. They may be downloaded and/or printed for private study, or other acts as permitted by national copyright laws. The publisher or other rights holders may allow further reproduction and re-use of the full text version. This is indicated by the licence information on the White Rose Research Online record for the item.

Takedown
If you consider content in White Rose Research Online to be in breach of UK law, please notify us by emailing eprints@whiterose.ac.uk including the URL of the record and the reason for the withdrawal request.

UNIVERSITY OF LEEDS
University of Sheffield
UNIVERSITY of York

2,6-Di(pyrazol-1-yl)pyridine-4-carboxylate Esters with Alkyl Chain Substituents, and their Iron(II) Complexes

Iurii Galadzhun[†], Rafal Kulmaczewski[†], Oscar Cespedes[‡], Mihoko Yamada[¶,§], Nobuto Yoshinari[¶], Takumi Konno[¶] and Malcolm A. Halcrow[,†]*

[†]School of Chemistry, University of Leeds, Woodhouse Lane, Leeds LS2 9JT, UK.

[‡]School of Physics and Astronomy, University of Leeds, E. C. Stoner Building, Leeds LS2 9JT, UK

[¶]Department of Chemistry, Graduate School of Science, Osaka University, Toyonaka, Osaka 560-0043, Japan.

[§]Current address: Division of Material Science, Graduate School of Science and Technology, Nara Institute of Science and Technology, Ikoma, Nara 630-0192, Japan.

ABSTRACT

Two series of 4-(alkoxyphenyl) 2,6-di{pyrazol-1-yl}pyridine-4-carboxyate (L^3R) or alkyl 2,6-di{pyrazol-1-yl}pyridine-4-carboxyate (L^4R) esters have been synthesized and complexed to iron(II), where R = C_nH_{2n+1} (n = 6, 12, 14, 16 or 18); two other derivatives related to L^3R are also reported. While the solid $[Fe(L^4R)_2][BF_4]_2$ compounds are isostructural by powder diffraction and show similar spin state behaviors, the $[Fe(L^3R)_2][BF_4]_2$ series shows more varied structures and magnetic properties. This was confirmed by solvated crystal structures of $[Fe(L^3R)_2][BF_4]_2$ with n = 6, 14 and 16, which all adopt the $P\bar{1}$ space group but show significantly different side-chain conformations and/or crystal packing. The solid complexes are mostly low-spin at room temperature, with many exhibiting the onset of thermal spin-crossover (SCO) upon warming. Heating the complexes with $n \geq 14$ significantly above their SCO temperature transforms them irreversibly into a predominantly high-spin state, which is accompanied by structure changes and loss of crystallinity by powder diffraction. These transformations do not coincide with lattice solvent loss, and may reflect melting and refreezing of their alkyl chain conformations during the thermal cycle. Four of the complexes exhibit SCO in CD_3CN solution with $T_{½}$ = 273-277 K, which is apparently unaffected by their alkyl chain substituents.

Introduction

Complexes derived from $[Fe(bpp)_2]^{2+}$ (bpp = 2,6-di{pyrazol-1-yl}pyridine, Chart 1)[1-3] are widely studied in spin-crossover (SCO) research.[4-6] Synthetic routes have been developed to incorporate carbon or heteroatom substituents to every position of the bpp skeleton.[7,8] Functionalization of the pyridyl *C*4 position is particularly useful, for introducing functional substituents or tether groups with no steric consequences for the metal ion. Thus, $[Fe(bpp)_2]^{2+}$ derivatives bearing redox-active,[9] conducting,[10] fluorescent,[11,12] photoisomerizable,[13] magnetically active[14] or metal-binding[12,14,15] substituents have been produced, in many cases yielding dual SCO switching functionality. Alternatively, bpp ligands and complexes with suitable tether groups have been deposited onto gold[16] or graphite[17] surfaces, or in single molecule junctions.[18]

Chart 1 Ligands referred to in this work (*m*, *n* = 6, 12, 14, 16 or 18).

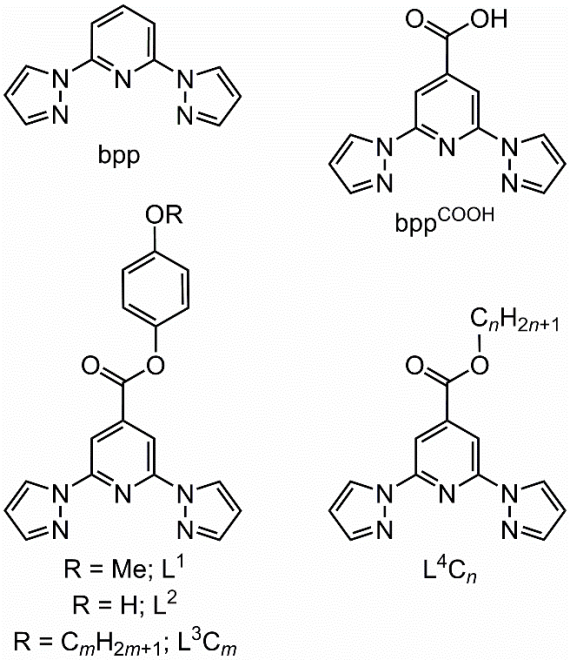

An important area where the $[Fe(bpp)_2]^{2+}$ family has not been much applied so far, however, is in SCO soft materials.[19] Many established SCO centers have been derivatized with long chain alkyl substituents and screened for mesogenic behavior.[20] Although a few genuine SCO liquid crystals are known,[21] it is

more common for SCO to occur concomitantly with a crystal-to-liquid-crystal (C→LC) phase change[22-27] or with isotropic melting.[28] These phenomena sometimes lead to abrupt spin-transitions.[26-28] However, the alkyl substituents can also act as inert spacers between the SCO centers in a material,[29] leading to gradual SCO switching[30,31] that is only slightly perturbed by a change of state, where this is observed.[22-25] Alternatively, SCO switching and liquid crystallinity may simply occur over different temperature ranges.[32,33] Where mesophase formation does not occur, changes in alkyl group conformation or disorder in the solid phase can also induce hysteretic SCO[34] or other novel properties. An example of the latter is low→high-spin "reverse SCO" on cooling, whose intrinsically unfavorable electronic and vibrational entropy can be offset by an increased conformational disorder in the alkyl chain substituents.[23,35,36] SCO complexes with alkyl chain substituents have also been used in switchable Langmuir-Blodgett films and other amphiphile assemblies.[20]

To probe the utility of $[Fe(bpp)_2]^{2+}$ centers in this area, we have synthesized two series of esters from 2,6-di{pyrazol-1-yl}pyridine-4-carboxyate (bpp^{COOH}, Chart 1) and their iron(II) complexes.[14,37] These were selected because previous work implied the bpp carboxy substituents should stabilize the low-spin form of the complexes,[8] promoting SCO at higher temperatures which might coincide with mesophase formation on heating.[22-26] Complexes of two other related ligands lacking long-chain substituents, L^1 and L^2 (Chart 1), are also described. The synthesis of L^4C_{18} has been briefly reported in a previous study.[37]

Experimental

Synthetic procedures and characterization data for the new organic ligands are given in the Supporting Information.

Synthesis of the iron complexes. All the iron(II) complexes were prepared using the following general procedure. Solutions of the appropriate ligand (0.5 mmol) in 1,2-dichloroethane (25 cm^3), and $Fe[BF_4]_2 \cdot 6H_2O$ (0.25 mmol) in acetone (20 cm^3), were mixed and briefly stirred at room temperature. The

yellow-brown solution was then concentrated to *ca* 50 % its original volume. Slow diffusion of *n*-pentane into the filtered solution yielded the complex as a red powder which was collected, and washed copiously with pentane before drying. Multiple recrystallization were often required to obtain the product in analytical purity. Crystallized yields were in the range of 30-70 %, depending on the solubility of the complex. Analytical data:

For $[Fe(L^1)_2][BF_4]_2$. Recrystallized from acetonitrile/diethyl ether. Elemental analysis for $C_{38}H_{30}B_2F_8FeN_{10}O_6$ found (calcd) (%) C 47.5 (47.9), H 3.10 (3.18), N 14.8 (14.7). ^{1}H NMR (CD_3CN) δ 3.9 (s, 6H, OCH_3), 7.1 (d, 7 Hz, 4H, Ph $H^{3/5}$), 7.5 (d, 7 Hz, 4H, Ph $H^{2/6}$), 23.1, 26.2 (both 4H, Py $H^{3/5}$ & Pz H^5), 39.8, 40.4 (both 4H, Pz H^3 + H^4).

For $[Fe(L^2)_2][BF_4]_2$. Recrystallized from acetonitrile/diethyl ether. Elemental analysis for $C_{36}H_{26}B_2F_8FeN_{10}O_6$ found (calcd) (%) C 46.7 (46.8), H 3.00 (2.84), N 15.3 (15.2). ^{1}H NMR (CD_3CN) δ 7.0 (br s, 4H, Ph $H^{3/5}$), 7.2 (br s, 2H, OH), 7.4 (br s, 4H, Ph $H^{2/6}$), 23.1, 26.4 (both 4H, Py $H^{3/5}$ & Pz H^5), 39.6, 40.7 (both 4H, Pz H^3 + H^4).

For $[Fe(L^3C_6)_2][BF_4]_2\cdot C_2H_4Cl_2$. Recrystallized from 1,2-dichloroethane/pentane. Elemental analysis for $C_{48}H_{50}B_2F_8FeN_{10}O_6\cdot C_2H_4Cl_2$ found (calcd) (%) C 50.2 (50.4), H 4.15 (4.57), N 12.1 (11.8). ^{1}H NMR (1:1 $CDCl_3$:CD_3CN) δ 0.9 (6H), 1.3 (4H), 1.4 (4H), 1.5 (4H), 1.8 (4H), 4.0 (4H, Ak C$^1H_2$), 7.1, 7.5 (both 4H, phenylene $H^{2/6}$ + $H^{3/5}$), 24.1, 27.2 (both 4H, Py $H^{3/5}$ & Pz H^5), 41.3, 42.4 (both 4H, Pz H^3 + H^4). The presence of 1,2-dichloroethane as lattice solvent is supported by the TGA of this material (Figure S46). However, single crystals that were obtained by slow evaporation from the same solvent instead contain lattice water. Elemental analysis for $C_{48}H_{50}B_2F_8FeN_{10}O_6\cdot H_2O$ found (calcd) (%) C 51.2 (51.9), H 4.20 (4.72), N 12.5 (12.6).

For $[Fe(L^3C_{12})_2][BF_4]_2\cdot H_2O$. Recrystallized from 1,2-dichloroethane/pentane. Elemental analysis for $C_{60}H_{74}B_2F_8FeN_{10}O_6\cdot H_2O$ found (calcd) (%) C 55.9 (56.4), H 5.75 (5.99), N 11.0 (11.0). ^{1}H NMR (1:1 $CDCl_3$:CD_3CN) δ 0.9 (6H), 1.3 (16H), 1.5 (4H), 1.7 (4H), 1.9 (4H), 2.1 (4H), 3.6 (4H), 3.8 (4H), 4.1 (4H,

Ak C^1H_2), 7.1, 7.5 (both 4H, phenylene $H^{2/6}$ + $H^{3/5}$), 23.0, 26.2 (both 4H, Py $H^{3/5}$ & Pz H^5), 39.4, 40.1 (both 4H, Pz H^3 + H^4).

For $[Fe(L^3C_{14})_2][BF_4]_2$. Recrystallized from 1,2-dichloroethane/pentane. Elemental analysis for $C_{64}H_{82}B_2F_8FeN_{10}O_6$ found (calcd) (%) C 58.2 (58.4), H, 6.19 (6.28), N, 10.7 (10.6). ^{1}H NMR (1:1 $CDCl_3$:CD_3CN) δ 0.9 (6H), 1.2 (28H), 1.5 (4H), 1.8 (4H), 1.9 (8H), 3.6 (4H), 4.0 (4H, Ak C^1H_2), 7.0, 7.5 (both 4H, phenylene $H^{2/6}$ + $H^{3/5}$), 24.3, 27.2 (both 4H, Py $H^{3/5}$ & Pz H^5), 41.3, 42.6 (both 4H, Pz H^3 + H^4).

For $[Fe(L^3C_{16})_2][BF_4]_2$. Recrystallized from 1,2-dichloroethane/pentane. Elemental analysis for $C_{68}H_{90}B_2F_8FeN_{10}O_6$ found (calcd) (%) C 59.3 (59.5), H, 6.67 (6.61), N, 10.1 (10.2). ^{1}H NMR (1:1 $CDCl_3$:CD_3CN) δ 0.9 (6H), 1.2 (40H), 1.8 (4H), 1.9 (4H), 4.0 (4H), 5.5 (8H), 7.0, 7.3 (both 4H, phenylene $H^{2/6}$ + $H^{3/5}$), 24.6, 27.2 (both 4H, Py $H^{3/5}$ & Pz H^5), 41.4, 42.5 (both 4H, Pz H^3 + H^4).

For $[Fe(L^3C_{18})_2][BF_4]_2$. Recrystallized from 1,2-dichloroethane/pentane. Elemental analysis for $C_{72}H_{98}B_2F_8FeN_{10}O_6$ found (calcd) (%) C 60.4 (60.5), H, 7.04 (6.91), N, 9.9 (9.8). ^{1}H NMR (1:1 $CDCl_3$:CD_3CN) δ 0.8 (6H), 1.2 (48H), 1.4 (8H), 1.7 (4H), 1.9 (4H), 3.9 (4H), 6.9, 7.3 (both 4H, phenylene $H^{2/6}$ + $H^{3/5}$), 24.7, 27.1 (both 4H, Py $H^{3/5}$ & Pz H^5), 41.3, 42.9 (both 4H, Pz H^3 + H^4).

For $[Fe(L^4C_{12})_2][BF_4]_2$. Recrystallized from 1,2-dichloroethane/pentane. Elemental analysis for $C_{48}H_{66}B_2F_8FeN_{10}O_4$ found (calcd) (%) C 53.4 (53.6), H, 6.33 (6.18), N, 12.9 (13.0). ^{1}H NMR (1:1 $CDCl_3$:CD_3CN) δ 0.9 (6H), 1.3 (28H), 1.6 (4H), 2.1 (4H), 2.6 (4H), 4.6 (4H, Ak C^1H_2), 22.6, 25.9 (both 4H, Py $H^{3/5}$ & Pz H^5), 38.7, 39.6 (both 4H, Pz H^3 + H^4).

For $[Fe(L^4C_{14})_2][BF_4]_2$. Recrystallized from 1,2-dichloroethane/pentane. Elemental analysis for $C_{52}H_{74}B_2F_8FeN_{10}O_4$ found (calcd) (%) C 54.9 (55.1), H, 6.46 (6.58), N, 12.2 (12.4). ^{1}H NMR (1:1 $CDCl_3$:CD_3CN) δ 0.9 (6H), 1.3 (28H), 1.6 (4H), 1.9 (12H), 3.0 (4H), 4.6 (4H, Ak C^1H_2), 24.3, 27.2 (both 4H, Py $H^{3/5}$ & Pz H^5), 41.3, 42.6 (both 4H, Pz H^3 + H^4).

For $[Fe(L^4C_{16})_2][BF_4]_2$. Recrystallized from 1,2-dichloroethane/pentane. Elemental analysis for $C_{56}H_{82}B_2F_8FeN_{10}O_4$ found (calcd) (%) C 56.5 (56.6), H, 6.79 (6.95), N, 11.6 (11.8). ^{1}H NMR (1:1

$CDCl_3$:CD_3CN) δ 0.9 (6H), 1.2 (32H), 1.6 (4H), 1.9 (12H), 2.6 (8H), 4.5 (4H), 22.7, 26.1 (both 4H, Py $H^{3/5}$ & Pz H^5), 39.1, 39.8 (both 4H, Pz H^3 + H^4).

For $[Fe(L^4C_{18})_2][BF_4]_2$. Recrystallized from 1,2-dichloroethane/pentane. Elemental analysis for $C_{60}H_{90}B_2F_8FeN_{10}O_4 \cdot 2H_2O$ found (calcd) (%) C 55.9 (56.3), H, 7.71 (7.40), N, 10.9 (10.9). ^{1}H NMR (1:1 $CDCl_3$:CD_3CN) δ 0.9 (6H), 1.3 (36H), 1.6 (4H), 1.9 (16H), 3.2 (8H), 4.5 (4H), 22.7, 26.0 (both 4H, Py $H^{3/5}$ & Pz H^5), 39.1, 39.8 (both 4H, Pz H^3 + H^4).

Single crystal X-ray structure determinations

Crystals of L^3C_{14} and $[Fe(L^3C_{14})_2][BF_4]_2 \cdot 2MeCN$ formed from the same solution of the complex in CD_3CN, after standing inside an NMR tube. Crystals of $[Fe(L^3C_6)_2][BF_4]_2 \cdot H_2O$ were obtained following slow evaporation of a dilute 1,2-dichloroethane solution of that compound over a period of weeks. Single crystals of the other compounds were grown from deuterochloroform solution (L^3C_{12}, L^4C_{12}); from acetone/pentane solvent mixtures (bpp^{COOH}, L^1, L^2, $[Fe(L^3C_{16})_2][BF_4]_2 \cdot H_2O$); or from acetonitrile solution using diethyl ether vapor as antisolvent ($[Fe(L^1)_2][BF_4]_2$, $[Fe(L^2)_2][BF_4]_2$). Diffraction data for L^3C_{12}, L^3C_{14} and $[Fe(L^3C_{14})_2][BF_4]_2 \cdot 2MeCN$ were recorded at station I19 of the Diamond synchrotron (λ = 0.6998 Å). This was necessary owing to their weak diffraction, which may be a consequence of their small crystal size and (for the L^3C_m crystals) thin needle morphology. All the other crystallographic data were measured with an Agilent Supernova dual-source diffractometer, using monochromated Cu-K_α (λ = 1.5418 Å) or Mo-K_α (λ = 0.7107 Å) radiation. The diffractometer was fitted with an Oxford Cryostream low-temperature device. Experimental details of the structure determinations are listed in Tables 1, S1 and S2. The structures were all solved by direct methods (*SHELXS97*[38]), and developed by full least-squares refinement on F^2 (*SHELXL97*[38]). Crystallographic figures were prepared using *XSEED*.[39]

No disorder is present in the ligand crystal structures, or in $[Fe(L^3C_{14})_2][BF_4]_2 \cdot 2MeCN$. All their non-H atoms were refined anisotropically, and H atoms were placed in calculated positions and refined using a riding model. The absolute structure of L^4C_{12}, which adopts a handed space group, could not be

unambiguously determined owing to the light atom composition of the crystal. Hence the Friedel opposite reflections in those datasets were merged for the final least squares cycles.

One BF_4^- ion in $[Fe(L^3C_6)_2][BF_4]_2{\cdot}H_2O$ is disordered about three sites, which were treated with refined B–F and F...F distance restraints. One hexoxy substituent was also refined over two orientations with a 0.67:0.33 occupancy ratio, using fixed C–O, C–C and 1,3-C...C distance restraints. One of the water H atoms was located in the Fourier map and refined, with the fixed restraint O–H = 0.90(2) Å and U_{iso} = 1.5x U_{eq}{O}. The other water H atom has no obvious hydrogen bond acceptor and was not located or refined, but is included in the molecular weight and density calculation.

Minor disorder about a B–F axis in one of the anions in $[Fe(L^3C_{16})_2][BF_4]_2{\cdot}H_2O$ was modelled over two orientations, with a refined occupancy ratio of 0.81:0.19. Refined B–F and F...F distance restraints were applied to this disorder. All non-H atoms except the minor anion disorder site were refined anisotropically. Both water H atoms were located in the Fourier map and refined described as above.

The other crystallographic refinement procedures are described in the Supporting Information.

Other measurements

Elemental microanalyses were performed by the microanalytical services at the University of Leeds School of Chemistry, or the London Metropolitan University School of Human Sciences. Electrospray mass spectra were recorded on a Bruker MicroTOF-q instrument from $CHCl_3$ solution. Diamagnetic NMR spectra employed a Bruker Ascend Advance III spectrometer operating at 400.1 MHz (^{1}H) or 100.6 MHz (^{13}C), while paramagnetic ^{1}H NMR spectra were obtained with a Bruker DPX300 spectrometer operating at 300.1 MHz. Thermogravimetric analyses employed a TA Instruments TGA Q50 analyser with a temperature ramp of 10 Kmin^{-1} under a stream of nitrogen gas. Differential scanning calorimetry (DSC) measurements used a TA Instruments DSC Q20 calorimeter, heating at a rate of 10 K min^{-1}. X-ray powder diffraction measurements were obtained at room temperature from a Bruker D2 Phaser diffractometer, using Cu-K_α radiation (λ = 1.5419 Å).

Table 1 Experimental details for the long chain alkyl-substituted compounds in this work. Other crystallographic data are listed in Tables S1 and S2.

	L^3C_{12}	L^3C_{14}	L^4C_{12}	$[Fe(L^3C_6)_2][BF_4]_2\cdot H_2O$	$[Fe(L^3C_{14})_2][BF_4]_2\cdot 2MeCN$	$[Fe(L^3C_{16})_2][BF_4]_2\cdot H_2O$
formula	$C_{30}H_{37}N_5O_3$	$C_{32}H_{41}N_5O_3$	$C_{24}H_{33}N_5O_2$	$C_{48}H_{52}B_2F_8FeN_{10}O_7$	$C_{68}H_{88}B_2F_8FeN_{12}O_6$	$C_{68}H_{92}B_2F_8FeN_{10}O_7$
fw	515.65	543.70	423.55	1110.47	1398.97	1390.99
cryst syst	monoclinic	monoclinic	orthorhombic	triclinic	triclinic	triclinic
space group	$P2_1/n$	$P2_1/n$	$P2_12_12_1$	$P\bar{1}$	$P\bar{1}$	$P\bar{1}$
a / Å	4.0957(1)	4.1217(1)	4.8115(2)	10.3052(8)	14.3159(1)	13.2899(3)
b / Å	64.302(1)	68.6161(7)	8.9659(7)	15.1497(10)	15.2193(1)	13.6465(4)
c / Å	10.3523(2)	10.3199(1)	53.569(3)	16.7305(9)	16.7869(2)	19.4605(6)
α / deg	90	90	90	89.147(5)	84.009(1)	98.865(2)
β / deg	96.680(2)	96.811(1)	90	77.068(6)	89.718(1)	91.201(2)
γ / deg	90	90	90	82.391(6)	72.722(1)	98.421(2)
V / Å^3	2707.91(9)	2898.02(8)	2310.9(2)	2523.0(3)	3472.07(5)	3446.19(17)
Z	4	4	4	2	2	2
T / K	100(2)	100(2)	120(2)	120(2)	100(2)	120(2)
μ / mm^{-1}	0.083[c]	0.081[c]	0.632[d]	3.193[d]	0.299[c]	0.301[e]
D_{calcd} / gcm^{-3}	1.265	1.246	1.217	1.462	1.338	1.340
reflns collected	10503	45669	5750	21089	74693	51010
unique reflns	3811	13562	2684	9509	31292	16785

R_{int}	0.082	0.071	0.053	0.059	0.051	0.048
$R_1, I > 2\sigma(I)$[a]	0.071	0.058	0.063	0.071	0.051	0.052
wR_2, all data[b]	0.194	0.155	0.175	0.196	0.142	0.120
GOF	1.071	0.904	1.058	1.040	0.951	1.026
Flack parameter	–	–	0.1(7)[f]	–	–	–

[a]$R = \Sigma\ [|F_o| - |F_c|]\ /\ \Sigma|F_o|$. [b]$wR = [\Sigma w(F_o^2 - F_c^2)^2\ /\ \Sigma wF_o^4]^{1/2}$. [c]Collected with synchrotron radiation. [d]Collected with Cu-K_a radiation. [e]Collected with Mo-K_a radiation. [f]The absolute structure of this light atom crystal was not determined.

Magnetic susceptibility measurements were performed using Quantum Design SQUID or VSM SQUID magnetometers, in an applied field of 5000 G with a temperature ramp of 5 $Kmin^{-1}$. Diamagnetic corrections for the samples were estimated from Pascal's constants.[40] Susceptibility measurements in solution were obtained by Evans method using a Bruker Avance 500 FT spectrometer operating at 500.1 MHz.[41] A diamagnetic correction for the sample,[40] and a correction for the variation of the density of the CD_3CN solvent with temperature,[42] were applied to these data. Thermodynamic parameters and spin-crossover midpoint temperatures were derived by fitting these data to eq 1 and 2, where nHS(T) is the high-spin fraction of the sample at temperature T:[43]

$$\ln[(1-n\mathrm{HS}(T))/n\mathrm{HS}(T)] = \Delta H/RT - \Delta S/R \qquad (1)$$

$$\Delta S = \Delta H/T_{½} \qquad (2)$$

Results and Discussion

Our initial attempts to prepare L^3C_m involved esterification of bpp^{COOH} [37] with 4-methoxyphenol to form L^1, which was then demethylated to L^2 with BBr_3. However, treatment of L^2 with alkyl iodides under basic conditions led to cleavage of the ester linkage, regenerating bpp^{COOH} as the major product. Hence, L^3C_m were instead prepared by an alternative route, of treating bpp^{COOH} with preformed 4-alkoxyphenol[44] using 4-(dimethylamino)pyridine (DMAP) as coupling reagent. This method afforded L^3C_m (m = 6, 12, 14, 16 or 18) in yields of 15-60 %, the lower yields reflecting solubility losses during purification. The alkyl esters L^4C_n were obtained in similar yields by treating bpp^{COOH} with the appropriate primary alcohol and DMAP, as before.

X-ray structure refinements were obtained for bpp^{COOH}, L^1, L^2, L^3C_{12}, L^3C_{14} and L^4C_{12}. Crystals of bpp^{COOH} and L^1 are isomorphs in the orthorhombic space group $Pna2_1$, despite their

different molecular structures and hydrogen bonding characteristics (Figures S14 and S16), while L^3C_{12} and L^3C_{14} are isostructural (monoclinic, $P2_1/n$). The alkoxy chains in L^3C_{12}, L^3C_{14} and L^4C_{12} (orthorhombic, $P2_12_12_1$) all adopt extended conformations in the crystal. However, while the L^4C_{12} molecule is almost planar in its overall shape, the phenylene spacers in L^3C_{12} and L^3C_{14} give those molecules a bent conformation about the carboxy pivot group. The heterocyclic groups in each compound form $\pi\ldots\pi$ stacks by translation along the unit cell *a* direction, which are grouped into bilayers related by crystallographic *m* symmetry in L^3C_{12} and L^3C_{14}, and by 2_1 symmetry in L^4C_{12} (Figures 1, 2, S20 and S21). Adjacent bilayers associate by interdigitation of their alkyl chains, giving V-shaped arrays of alternating heterocyclic and alkyl domains. The dihedral angle between the (almost planar) heterocyclic regions of the molecular stacks in each bilayer is 34.24(4)° in L^3C_{12}, 34.20(2)° in L^3C_{14} and 86.31(4)° in L^4C_{12}. Hence, the molecular stacks in L^4C_{12} are more canted with respect to their neighbors than in the L^3C_m crystals.

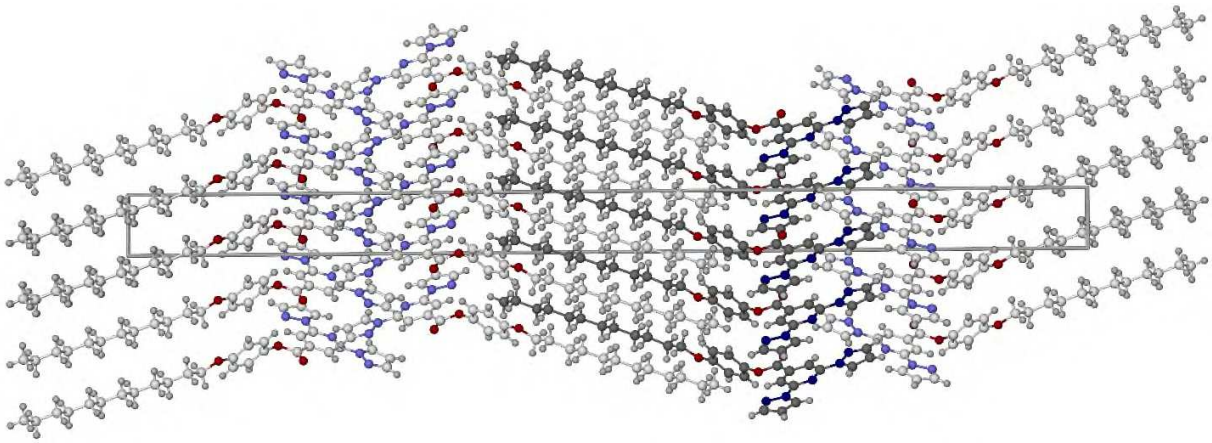

Figure 1 Packing diagram of L^3C_{12}. One molecular stack is highlighted with dark coloration, for clarity. The view is parallel to the [001] crystallographic vector, with *b* horizontal. Color code C, white or dark grey; H, pale grey; N, pale or dark blue; O, red.

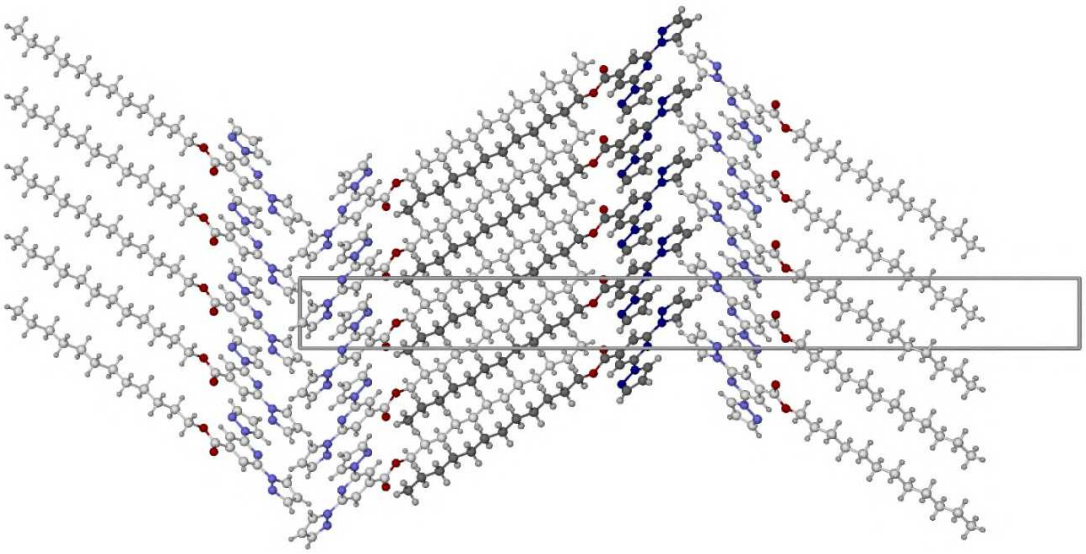

Figure 2 Packing diagram of L^4C_{12}. One molecular stack is highlighted with dark coloration, for clarity. The view is parallel to the [010] crystallographic vector, with *c* horizontal. Color code C, white or dark grey; H, pale grey; N, pale or dark blue; O, red.

The L^4C_n materials are all isostructural by powder diffraction and/or crystallographic unit cell measurements. Solid L^3C_{12}, L^3C_{14} and L^3C_{16} are also isostructural, but the powder patterns of L^3C_6 and L^3C_{18} are less informative owing to poor crystallinity (Figures S22-S25). All these compounds undergo reversible isotropic melting at temperatures between 109-118 °C (L^3C_m) and 78-91 °C (L^4C_n), with no evidence of mesophase formation by DSC (Figures S27-S28) or optical microscopy.

Homoleptic iron(II) complexes of each new ligand were prepared as their BF_4^- salts. Purification of these compounds was often challenging owing to their solubility characteristics, but all the complexes except $[Fe(L^4C_6)_2][BF_4]_2$ (which is not described further) were obtained in analytical purity after recrystallization from 1,2-dichloroethane (dce)/pentane or (for

$[Fe(L^1)_2][BF_4]_2$ and $[Fe(L^2)_2][BF_4]_2$) from acetonitrile/diethyl ether. All characterization of the bulk materials was performed using samples isolated from these solvent mixtures. While the $[Fe(L^4C_n)_2][BF_4]_2$ materials are mostly solvent-free, the $[Fe(L^3C_m)_2][BF_4]_2$ series often contain lattice water or organic solvents by crystallography, TGA and/or microanalysis. The solvent content seems to vary in different samples of the same compound, particularly in $[Fe(L^3C_6)_2][BF_4]_2$ which reproducibly contains *ca* 1 equiv lattice dce when rapidly precipitated from dce, but whose single crystals grown by slow evaporation from the same solvent have a monohydrate formulation. These different formulations were confirmed by TGA (Figure S46), but have little effect on the structure of the material by X-ray powder diffraction (Figure S41). The solvent in $[Fe(L^3C_m)_2][BF_4]_2$ can often be removed *in vacuo*, although this may induce a structural phase change (see below). In view of their variable solvent content, this series of complexes is referred to in the following discussions as $[Fe(L^3C_m)_2][BF_4]_2{\cdot}x$solv, or as $[Fe(L^3C_m)_2][BF_4]_2{\cdot}xH_2O$ when the hydrate compounds are considered specifically.

Crystal structures were obtained of $[Fe(L^1)_2][BF_4]_2$, $[Fe(L^2)_2][BF_4]_2$ and three $[Fe(L^3C_m)_2][BF_4]_2{\cdot}x$solv compounds: $[Fe(L^3C_6)_2][BF_4]_2{\cdot}H_2O$, $[Fe(L^3C_{14})_2][BF_4]_2{\cdot}2$MeCN and $[Fe(L^3C_{16})_2][BF_4]_2{\cdot}H_2O$.[45] All five crystalline complexes are low-spin at 120 K, as expected from their magnetic susceptibility data (see below). While the $[Fe(L^3C_m)_2][BF_4]_2{\cdot}x$solv crystals each adopt the triclinic space group $P\overline{1}$, they differ in their alkyl chain conformations and/or molecular packing. The hexoxy substituents in $[Fe(L^3C_6)_2]^{2+}$ both have at least one *gauche* torsion, with one of them being crystallographically disordered. In contrast, $[Fe(L^3C_{14})_2]^{2+}$ and $[Fe(L^3C_{16})_2]^{2+}$ have perfectly extended alkoxy groups with all-*anti* torsions, and no sign of crystallographic disorder (Figures 3 and S32-S34). The complexes also differ in the orientations of the ligand phenylene groups. In $[Fe(L^3C_{14})_2]^{2+}$ and $[Fe(L^3C_{16})_2]^{2+}$, one phenylene ring is

perpendicular to its carboxy group while the two groups on the other ligand are coplanar. In contrast, both phenylene rings are (approximately) perpendicular to their carboxy linker in $[Fe(L^3C_6)_2]^{2+}$. That implies some conformational flexibility in the 4-alkoxyphenoxy substituents of these complexes. These differences have little apparent influence on the $[Fe(bpp)_2]^{2+}$ core of the compounds however, whose metric parameters are all typical for low-spin complexes of this type (Table S5).[1] The lattice water in the hydrate crystals is remote from the metal centers, and donates hydrogen bonds to the BF_4^- ions.

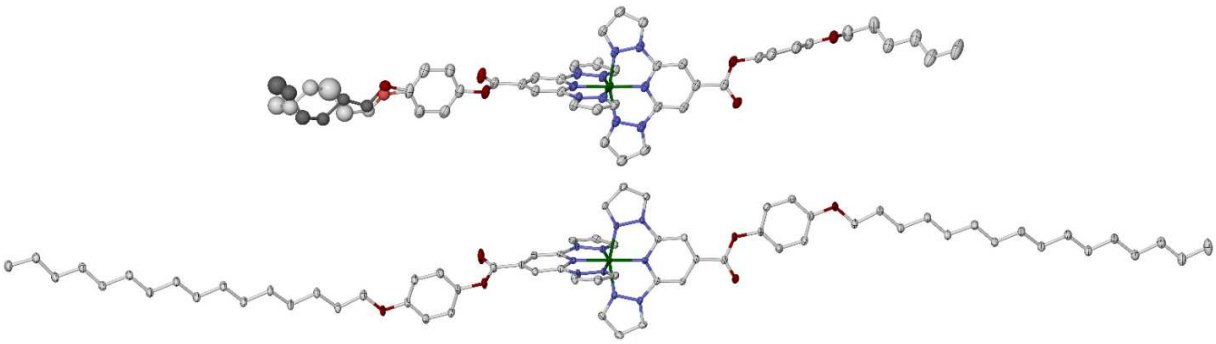

Figure 3 The complex dications in $[Fe(L^3C_6)_2][BF_4]_2{\cdot}H_2O$ (top) and $[Fe(L^3C_{16})_2][BF_4]_2{\cdot}H_2O$ (bottom). Displacement ellipsoids are at the 50 % probability level, and H atoms are omitted for clarity. The major and minor hexoxy group disorder sites in $[Fe(L^3C_6)_2]^{2+}$ are highlighted in dark and pale coloration, respectively. Color code C, white or dark grey; Fe, green; N, blue; O, red.

The metal/heterocyclic (Fe/bpp) cores in all three crystals form weak centrosymmetric dimers, with overlapping coplanar pyrazolyl rings separated by 3.431(9)-3.613(8) Å. In $[Fe(L^3C_{14})_2][BF_4]_2{\cdot}2MeCN$ and $[Fe(L^3C_{16})_2][BF_4]_2{\cdot}H_2O$ these cation dimers are arranged by translation into layers within the (001) crystal plane. These layers are separated by interdigitated alkoxy chains oriented at an angle of *ca* 25° to the plane of the layers (Figures 4 and S37-S39).

This packing motif requires all the phenylene spacer groups in the lattice to be approximately coplanar, which explains the different conformations of the two carboxyphenylene substituents in these molecules. The interlayer spacings in the structures are slightly smaller than the unit cell *c* dimensions, at 16.689(1) (*m* = 14) and 19.209(2) (*m* = 16) Å. The placement of anions and solvent in the two structures is also similar, apart from the second MeCN molecule in $[Fe(L^3C_{14})_2][BF_4]_2 \cdot 2MeCN$ which lies beside a BF_4^- ion in an enlarged cavity between the cation layers. That suggests space filling by additional solvent may be a requirement for these two crystals to adopt the same molecular association motif, despite their different alkoxy chain lengths. In contrast, there is no interdigitation of the hexyl groups in $[Fe(L^3C_6)_2][BF_4]_2 \cdot H_2O$, which has no segregation of the rigid and flexible moieties in the lattice (Figure S36).

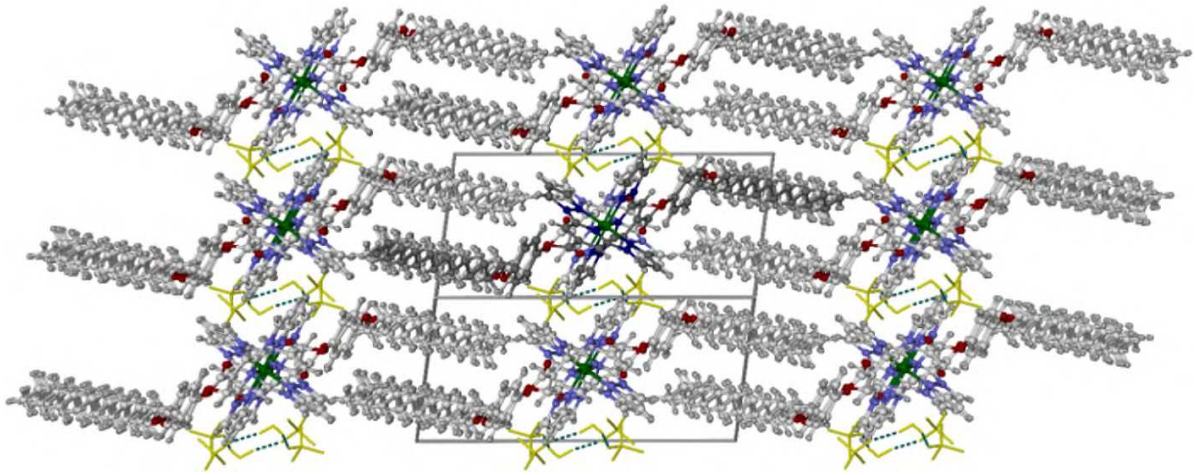

Figure 4 Packing diagram of $[Fe(L^3C_{16})_2][BF_4]_2 \cdot H_2O$, showing the association of the cations into layers parallel to the (001) crystal plane. Only one orientation of the disordered anion is shown. One cation is highlighted with dark coloration and the anions and solvent are de-emphasized, for clarity. The view is parallel to the $[\bar{1}10]$ vector, with *c* horizontal. Color code C, white or dark grey; H, pale grey; Fe, green; N, pale or dark blue; O, red; BF_4^- and H_2O, yellow.

Powder samples of each $[Fe(L^3C_m)_2][BF_4]_2 \cdot x$solv compound adopt a different structure, except m = 16 and 18 which appear isostructural (Figure S42). Moreover, these structures show a complicated dependence on the presence or absence of lattice solvent (see below). On one hand, powdered $[Fe(L^3C_{14})_2][BF_4]_2 \cdot xH_2O$ is not isostructural with its crystalline phase $[Fe(L^3C_{14})_2][BF_4]_2 \cdot 2MeCN$ (Figure S41).[45] That implies loss or replacement of the lattice solvent leads to structural changes in that compound (see below). Conversely, the powder patterns of crystalline $[Fe(L^3C_6)_2][BF_4]_2 \cdot H_2O$ and powdered $[Fe(L^3C_6)_2][BF_4]_2 \cdot C_2H_4Cl_2$ closely resemble each other, implying their solvent content has little effect on the structure of $[Fe(L^3C_6)_2][BF_4]_2 \cdot x$solv. In contrast, all the $[Fe(L^4C_n)_2][BF_4]_2$ compounds apparently adopt the same structure type by powder diffraction, which becomes more crystalline with longer chain lengths (Figure S43).

$[Fe(L^3C_m)_2][BF_4]_2 \cdot xH_2O$ show varied solid state magnetic properties, in keeping with their different powder diffraction structures. The materials with m = 6, 16 and 18 remain low-spin between 5-350 K, with the latter two compounds showing the onset of SCO between 350-370 K (Figure 5). However, when m = 14, the compound is low-spin at room temperature but shows a small, irreversible increase in $\chi_M T$ upon warming to 350 K, consistent with a low→high-spin conversion in about 10 % of the sample. That may be associated with loss of lattice water from the material, which occurs around 340 K by DSC and TGA (see below).[22,46] Finally, $[Fe(L^3C_{12})_2][BF_4]_2 \cdot xH_2O$ is the only solid compound with a significant high-spin population at room temperature when freshly isolated. Its $\chi_M T$ value of 2.2 $cm^3mol^{-1}K$ at 300 K implies *ca* 65 % of the sample is high-spin at that temperature. Around half this high-spin fraction exhibits a gradual, non-hysteretic SCO on cooling with $T_{½} \approx 210$ K; the onset of a second SCO event is also apparent above 370 K. Warming the freshly prepared sample to 370 K leads to a small,

permanent increase in its high-spin population without changing the form of the $\chi_M T$ *vs* T curve over that temperature range. A more pronounced form of the same behavior was found when the sample was rapidly cooled to 5 K, then remeasured (Figure S47). The initial $\chi_M T$ *vs* T curve of the quenched sample has a similar form as in Figure 5, but $\chi_M T$ rises more slowly upon warming from 5 K, reaching 1.9 $cm^3mol^{-1}K$ at 300 K which is 0.3 $cm^3mol^{-1}K$ lower than in the unquenched material. Upon further heating to 330 K $\chi_M T$ in the quenched sample increases more rapidly towards that of the unquenched material, and the cooling scans under both temperature programs are more similar.

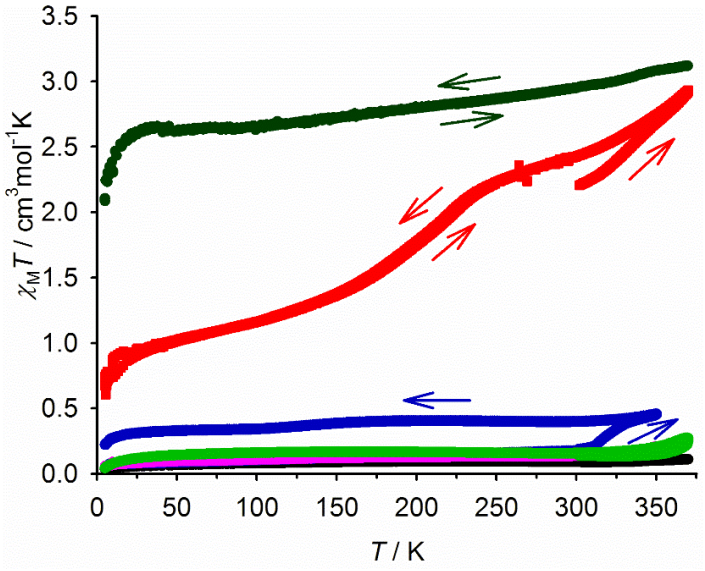

Figure 5 Magnetic susceptibility data for $[Fe(L^3C_6)_2][BF_4]_2{\cdot}xH_2O$ (black), $[Fe(L^3C_{12})_2][BF_4]_2{\cdot}xH_2O$ (red), $[Fe(L^3C_{14})_2][BF_4]_2{\cdot}xH_2O$ (blue), $[Fe(L^3C_{16})_2][BF_4]_2{\cdot}xH_2O$ (pale green) and $[Fe(L^3C_{18})_2][BF_4]_2{\cdot}xH_2O$ (pink). $[Fe(L^3C_{12})_2][BF_4]_2{\cdot}xH_2O$ was measured on a 300→370→3→300 K temperature cycle (see also Figure S47). The dark green curve shows a sample of $[Fe(L^3C_{16})_2][BF_4]_2{\cdot}xH_2O$ after annealing at 170 °C. All scan rates 5 $Kmin^{-1}$.

In contrast, solid $[Fe(L^1)_2][BF_4]_2$, $[Fe(L^2)_2][BF_4]_2$ and all the $[Fe(L^4C_n)_2][BF_4]_2$ series exhibit more consistent magnetic data, being low-spin between 5-250 K but with a slow increase in $\chi_M T$ on further warming that indicates the onset of SCO (Figure 6). This is best defined for $[Fe(L^4C_{14})_2][BF_4]_2$, whose SCO has a midpoint temperature ($T_{½}$) of 353 K and a small thermal hysteresis loop (ΔT = 10 K at its widest point) which is retained upon multiple cycling about the transition. The other materials show $T_{½}$ >370 K, with no hysteresis within the temperature range of the measurement. These data are consistent with salts of $[Fe(bpp^{COOH})_2]^{2+}$ and other $[Fe(bpp)_2]^{2+}$ derivatives bearing carboxy pyridyl substituents, which often undergo SCO above room temperature in the solid state.[8,14,47]

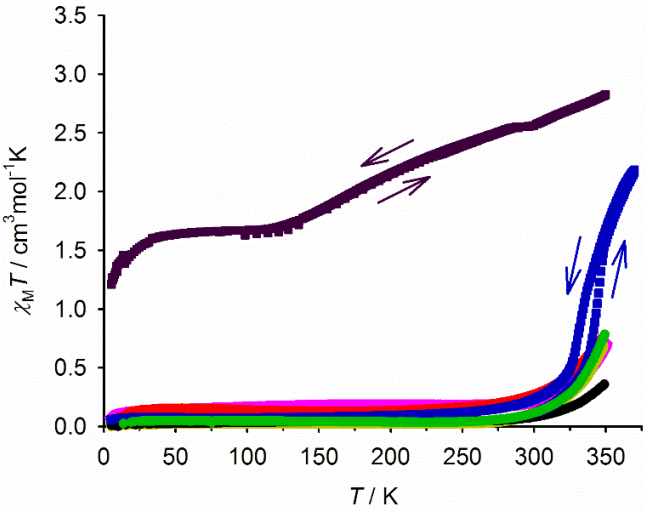

Figure 6 Magnetic susceptibility data for $[Fe(L^1)_2][BF_4]_2$ (black), $[Fe(L^2)_2][BF_4]_2$ (yellow), $[Fe(L^4C_{12})_2][BF_4]_2$ (red), $[Fe(L^4C_{14})_2][BF_4]_2$ (blue), $[Fe(L^4C_{16})_2][BF_4]_2$ (green) and $[Fe(L^4C_{18})_2][BF_4]_2$ (pink). The dark purple curve shows a sample of $[Fe(L^4C_{18})_2][BF_4]_2$ after annealing at 170 °C. All scan rates 5 Kmin^{-1}.

DSC data for the $[Fe(L^4C_n)_2][BF_4]_2$ series all show a single endotherm at 73±1°C (n = 14) or 92-95 °C (other compounds), which agree well with the SCO transition temperatures derived from the magnetic data (Figure S49). However, this is only reversible if the sample is kept below *ca* 120 °C. If the sample is scanned to higher temperatures, the SCO becomes irreversible and, for n = 18 only, is replaced by two new weak and reversible features near room temperature (Figure 7). DSCs of the $[Fe(L^3C_m)_2][BF_4]_2 \cdot xH_2O$ materials are again more complicated (Figure S48), and were interpreted by comparison with their magnetic, TGA and thermochromic behavior. The DSC of $[Fe(L^3C_6)_2][BF_4]_2 \cdot xH_2O$ is almost featureless, with no peak that might indicate SCO below 180 °C. In contrast, $[Fe(L^3C_{12})_2][BF_4]_2 \cdot xH_2O$ shows a weaker, fully reversible endotherm at 126 °C, which is consistent with the partial SCO evident in its magnetic data at high temperature (Figure 5). DSCs of $[Fe(L^3C_m)_2][BF_4]_2 \cdot xH_2O$ (m = 14, 16, 18) each exhibit two endotherms: one at 70-80 °C, which correlates with a mass loss of 1.5-2.0 % between 60-80 °C by TGA and can be attributed to loss of lattice water; and, another between 126-142 °C which can be assigned to SCO. Both endotherms in these three compounds are irreversible, and are replaced in the reverse scans by broad, weak features just above room temperature that resemble those in the high-temperature scan in Figure 7.

The irreversible changes to the DSC data upon heating the longer chain complexes were confirmed by magnetic measurements, on samples of one compound from each series that had been previously annealed at 170 °C (Figures 5 and 6). In contrast to the freshly prepared materials, the annealed samples were predominantly high-spin at room temperature, and underwent very gradual, ill-defined and incomplete SCO upon cooling to 5 K.

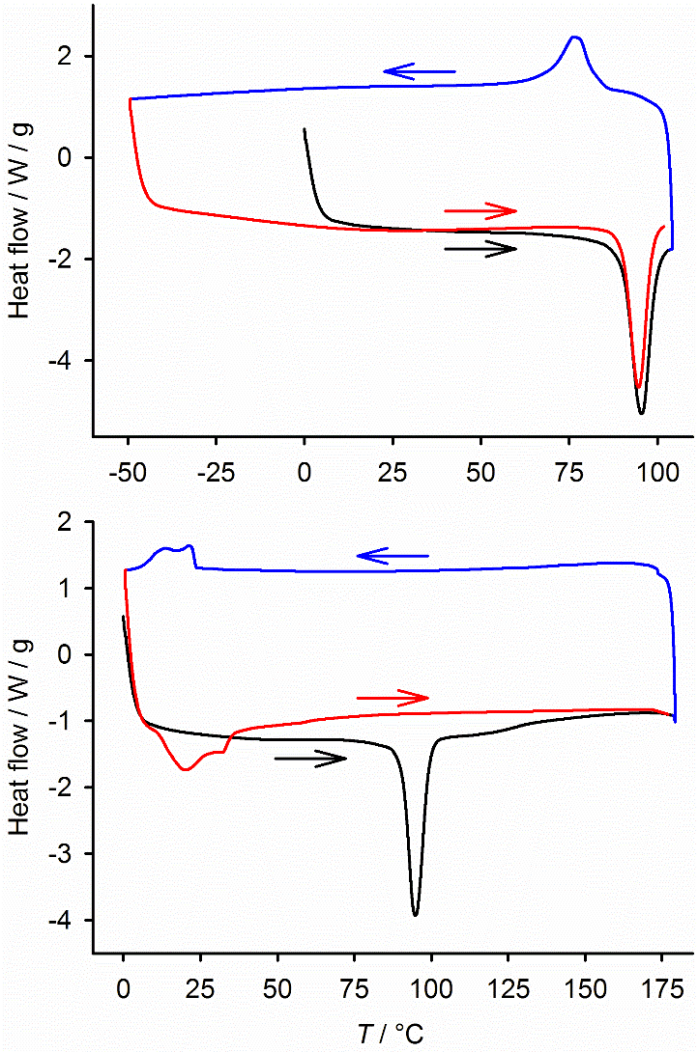

Figure 7 DSC data for $[Fe(L^4C_{18})_2][BF_4]_2$ measured over low-temperature (top) and high-temperature (bottom) ranges, where the SCO endotherm is respectively reversible and irreversible. Initial heating (black), initial cooling (blue) and second heating (red) temperature ramps are shown, at a scan rate of 10 $Kmin^{-1}$.

The effect of heating on the long chain complexes was probed further, by measuring X-ray powder patterns of samples after annealing for 15 mins at 100 or at 170 °C (Figure 8). The

annealing had little effect on $[Fe(L^3C_6)_2][BF_4]_2 \cdot xH_2O$ or $[Fe(L^3C_{12})_2][BF_4]_2 \cdot xH_2O$, but for $m \geq 14$ the samples showed large changes in their powder patterns after annealing at both temperatures, implying crystallographic phase changes (which could reflect loss of lattice water, see above) coupled to a general loss of crystallinity (Figure S44). In contrast all the $[Fe(L^4C_n)_2][BF_4]_2$ series behaved similarly, in showing little change after heating to 100 °C while the higher temperature annealing caused a reduction in crystallinity, which is more pronounced for the longer chain lengths (Figure S45). Similar irreversible phase changes on heating have been seen in some other SCO complexes bearing long chain alkyl substituents.[24]

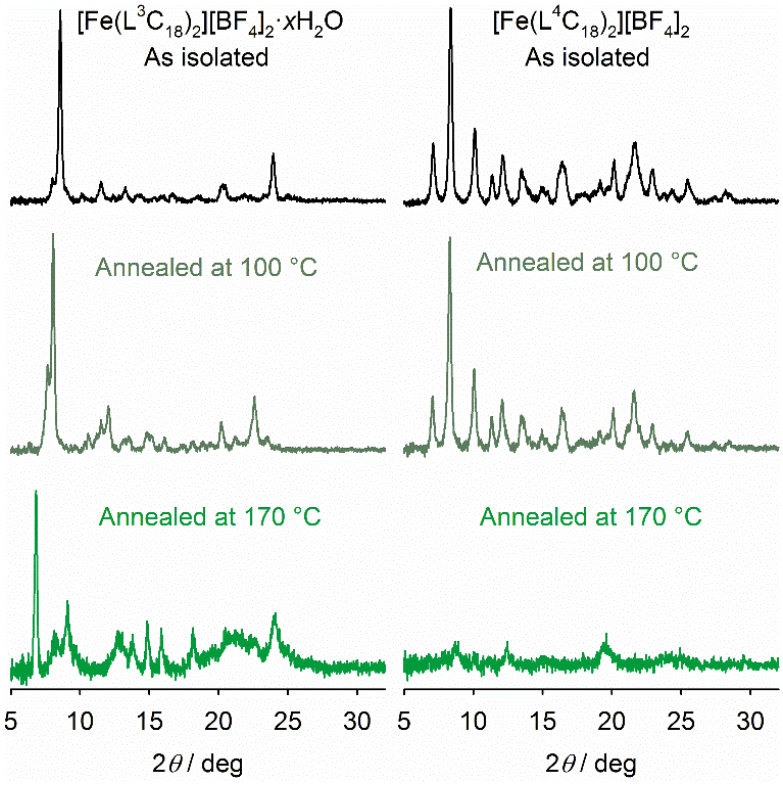

Figure 8 Room temperature X-ray powder patterns of $[Fe(L^3C_{18})_2][BF_4]_2 \cdot xH_2O$ and $[Fe(L^4C_{18})_2][BF_4]_2$, before and after annealing at different temperatures. Data for the other compounds from these series are in Figures S44 and S45.

Visual inspection of the long chain complexes on heating showed all of them except $[Fe(L^3C_6)_2][BF_4]_2 \cdot xH_2O$ undergo a gradual color change from brown to orange upon heating above 100 °C, which is consistent with the absence or presence of thermal SCO predicted by their magnetic and/or DSC data (Figures S50 and S51). However, all the compounds remain in the solid state at all temperatures up to 170 °C. Hence, changes in spin state behavior and loss of crystallinity upon heating the samples does not reflect mesophase formation or melting within the temperature range examined.[22-28]

Magnetic susceptibility data for four of the complexes in CD_3CN solution were also measured by Evans method (Figure S52).[41] Each compound undergo typical SCO equilibria in solution with midpoint temperatures between 273-277 K (Table 2; for comparison, $[Fe(bpp^{COOH})_2][BF_4]_2$ exhibits $T_{½}$ = 281 K under similar conditions[8]). Although there are small variations in the enthalpy and entropies of these equilibria, these are within the normal ranges for measurements of this type.[8,48] We conclude that the conformational entropy of the hexadecyl substituents in $[Fe(L^3C_{16})_2][BF_4]_2$ and $[Fe(L^4C_{16})_2][BF_4]_2$ has little influence on the progress of SCO in solution.

Table 2 SCO parameters in CD_3CN solution for four of the compounds in this work. The magnetic data and fits to derive the thermodynamic quantities are shown in Figure S52.

	$T_{½}$ / K	ΔH / kJmol^{-1}	ΔS / Jmol^{-1}K^{-1}
$[Fe(L^1C_{12})_2][BF_4]_2$	277(1)	26.6	96
$[Fe(L^2C_{12})_2][BF_4]_2$	277(1)	25.6	93
$[Fe(L^3C_{16})_2][BF_4]_2 \cdot xH_2O$	273(2)	22.3	81
$[Fe(L^4C_{16})_2][BF_4]_2$	275(2)	28.2	103

Conclusion

The first members of the $[Fe(bpp)_2]^{2+}$ family of SCO complexes bearing peripheral long chain substituents, have been synthesized from two series of bpp derivatives L^3C_m and L^4C_n. While $[Fe(L^4C_n)_2][BF_4]_2$ (n = 12, 14, 16, 18) are isostructural by powder diffraction and show quite similar spin state and phase behaviors at different temperatures, the $[Fe(L^3C_m)_2][BF_4]_2 \cdot x$solv series ($m$ = 6, 12, 14, 16, 18) show more varied structures and spin state properties in the solid state. This was confirmed by crystal structures of $[Fe(L^3C_6)_2][BF_4]_2 \cdot H_2O$ and $[Fe(L^3C_{16})_2][BF_4]_2 \cdot H_2O$, which are not isostructural and show quite different crystal packing motifs. A third crystalline solvate $[Fe(L^3C_{14})_2][BF_4]_2 \cdot 2MeCN$ was also obtained, whose molecular packing resembles $[Fe(L^3C_{16})_2][BF_4]_2 \cdot H_2O$ but is different from $[Fe(L^3C_{14})_2][BF_4]_2 \cdot xH_2O$ by powder diffraction. Conversely, the structures of $[Fe(L^3C_6)_2][BF_4]_2 \cdot H_2O$ and $[Fe(L^3C_6)_2][BF_4]_2 \cdot C_2H_4Cl_2$ are very similar by powder diffraction despite their different solvent content. Hence the structures of $[Fe(L^3C_m)_2][BF_4]_2 \cdot x$solv, and their dependence on the solvent present, differ strongly depending on m. With one exception ($[Fe(L^3C_{12})_2][BF_4]_2 \cdot xH_2O$) all the complexes in this work are low-spin at 298 K, and many of them undergo SCO on warming with $T_{½} \geq 350$ K. Four of the compounds also undergo SCO in CD_3CN solution, with almost identical $T_{½}$ values just below room temperature.

While none of the ligands or complexes formed mesophases under the conditions of measurement, some complexes bearing longer chain substituents convert irreversibly to a predominantly high-spin form upon heating above 420-440 K. This transformation is not connected to SCO for $[Fe(L^4C_n)_2][BF_4]_2$ ($n \geq 14$) which show $345 \leq T_{½} \leq 368$ K by DSC, since their SCO is reversible if the material is kept below 400 K but not after heating to 443 K (Figure 7). However, SCO itself is apparently irreversible in $[Fe(L^3C_m)_2][BF_4]_2 \cdot H_2O$ ($m \geq 14$), which

have higher $T_{½}$ values. Variable temperature magnetic data were collected for two annealed samples, which were predominantly high-spin and exhibited very gradual and incomplete SCO on cooling. Such ill-defined SCO is often found in amorphous materials.[29,49] Consistent with that, annealing the compounds at 443 K transforms them to new, poorly crystalline phases by powder diffraction.

While the $[Fe(L^3C_m)_2][BF_4]_2 \cdot xH_2O$ compounds contain variable amounts of lattice water, the irreversible spin-state changes are not directly caused by dehydration, which occurs at least 45 K below the SCO temperature.[22,46] Rather, they seem to be a function of the alkyl chain substituents in the molecules. The structural changes causing this behavior presumably involve conformational melting of the alkyl chains upon heating, which would then be frozen into a more random distribution of conformations upon recooling the sample. That process, which resembles the glass transition common in organic soft materials,[50] would explain the reduced crystallinity in the annealed materials (Figures 8, S44 and S45). Similar effects have been seen upon annealing other series of SCO complexes bearing long-chain substituents, which were also attributed to phase changes involving the alkyl chains.[24,30] Moreover DSC data from those literature compounds strongly resemble those in this work, including the ingrowth of weak reversible features close to room temperature after annealing.[24,30] Similar changes to the ligand conformations, at lower temperatures, can also account for the more complicated magnetic behavior of $[Fe(L^3C_{12})_2][BF_4]_2 \cdot xH_2O$ when thermally scanned from room temperature, and after rapid cooling (Figures 5 and S43).[33]

Finally, softening of the lattice during the annealing process might allow the some of the high-spin iron centers to isomerize to more distorted coordination geometries, reflecting Jahn-Teller distortion of the pentet high-spin iron(II) centers. These distortions are well-known to trap solid

$[Fe(bpp)_2]^{2+}$ derivatives in their high-spin form.[1,3,51] That could explain the predominantly high-spin state nature of the annealed samples, as well as the incompleteness of their thermal SCO (Figures 5 and 6). Stereochemically related $[Fe(terpy)_2]^{2+}$ derivatives, dispersed in liquid crystal matrices, show irreversible low→high-spin transitions above room temperature which might have a similar origin.[52]

Our current work aims to exploit the synthetic versatility of the bpp ligand family[7] to produce new iron(II) complexes decorated with alkyl chains at different sites on the ligand framework. The spin-states and phase behavior of these new compounds will be reported in future publications.

ASSOCIATED CONTENT

Supporting Information The following material is available free of charge via the Internet at http://pubs.acs.org.

Synthetic procedures and characterizatrion data for the organic ligands; experimental data, refinement procedures and tabulated metric parameters for the remaining crystal structure determinations; X-ray powder diffraction, TGA and DSC data; and additional solid state and solution phase magnetic susceptibility measurements (PDF).

X-ray crystal structures of the organic ligands: CCDC 1844095–1844099 and 1854266 (CIF).

X-ray crystal structures of the metal complexes: CCDC 1844100–1844103 and 1854267 (CIF).

Experimental data sets associated with this paper are available from the University of Leeds library (http://doi.org/10.5518/455).

AUTHOR INFORMATION

Corresponding Author

*Email: m.a.halcrow@leeds.ac.uk

ORCID

Iurii Galadzhun: 0000-0002-0512-3830

Rafal Kulmaczewski: 0000-0002-3855-4530

Oscar Cespedes: 0000-0002-5249-9523

Mihoko Yamada: 0000-0002-3789-6600

Nobuto Yoshinari: 0000-0003-2457-0967

Takumi Konno: 0000-0003-4612-5418

Malcolm A. Halcrow: 0000-0001-7491-9034

Notes

The authors declare no competing financial interest.

ACKNOWLEDGEMENTS

This work was funded by the the University of Leeds, the EPSRC (EP/K012568/1 and EP/K00512X/1), CREST and JST (JPMJCR13L3). We thank Diamond Light Source for access to beamline I19 (MT10334) that contributed to the results presented here.

REFERENCES

(1) Halcrow, M. A. Iron(II) Complexes of 2,6-Di(pyrazol-1-yl)pyridines – a Versatile System for Spin-Crossover Research. *Coord. Chem. Rev.* **2009**, *253*, 2493–2514.

(2) Olguín, J.; Brooker, S. Spin Crossover Active Iron(II) Complexes of Selected Pyrazole-Pyridine/Pyrazine Ligands. *Coord. Chem. Rev.* **2011**, *255*, 203–240.

(3) Kershaw Cook, L. J.; Mohammed, R.; Sherborne, G.; Roberts, T. D.; Alvarez, S.; Halcrow, M. A. Spin State Behaviour of Iron(II)/Dipyrazolylpyridine Complexes. New Insights from Crystallographic and Solution Measurements. *Coord. Chem. Rev.* **2015**, *289–290*, 2–12.

(4) Gütlich, P.; Goodwin, H. A. (eds.) *Spin Crossover in Transition Metal Compounds I−III, Topics in Current Chemistry*; Springer-Verlag: Berlin, 2004; Vols. 233–235.

(5) Halcrow, M. A. (ed), *Spin-Crossover Materials - Properties and Applications,* John Wiley & Sons, Ltd.: New York, 2013, p. 568.

(6) For recent general reviews of SCO chemistry see: (a) Sato, O. Dynamic Molecular Crystals with Switchable Physical Properties. *Nature Chem.* **2016**, *8*, 644–656. (b) Kumar, K. S.; Ruben, M. Emerging Trends in Spin Crossover (SCO) Based Functional Materials and Devices. *Coord. Chem. Rev.* **2017**, *346*, 176–205. (c) Molnár, G.; Rat, S.; Salmon, L.; Nicolazzi, W.; Bousseksou, A. Spin Crossover Nanomaterials: From Fundamental Concepts to Devices. *Adv. Mater.* **2018**, *30*, 17003862/1–23.

(7) Halcrow, M. A. Recent Advances in the Synthesis and Applications of 2,6-Dipyrazolylpyridine Derivatives and their Complexes. *New J. Chem.* **2014**, *38*, 1868–1882.

(8) Kershaw Cook, L. J.; Kulmaczewski, R.; Mohammed, R.; Dudley, S.; Barrett, S. A.; Little, M. A.; Deeth, R. J.; Halcrow, M. A. A Unified Treatment of the Relationship Between Ligand Substituents and Spin State in a Family of Iron(II) Complexes. *Angew. Chem. Int. Ed.* **2016**, *55*, 4327–4331.

(9) Nihei, M.; Han, L.; Oshio, H. Magnetic Bistability and Single-Crystal-to-Single-Crystal Transformation Induced by Guest Desorption. *J. Am. Chem. Soc.* **2007**, *129*, 5312–5313.

(10) Nihei, M.; Takahashi, N.; Nishikawa, H.; Oshio, H. Spin-Crossover Behavior and Electrical Conduction Property on Iron(II) Complexes with Tetrathiafulvalene Moieties. *Dalton Trans.* **2011**, *40*, 2154–2156.

(11) (a) González-Prieto, R.; Fleury, B.; Schramm, F.; Zoppellaro, G.; Chandrasekar, R.; Fuhr, O.; Lebedkin, S.; Kappes, M.; Ruben, M. Tuning the Spin-Transition Properties of Pyrene-Decorated 2,6-Bispyrazolylpyridine Based Fe(II) Complexes. *Dalton Trans.* **2011**, *40*, 7564–7570. (b) Santoro, A.; Kershaw Cook, L. J.; Kulmaczewski, R.; Barrett, S. A.; Cespedes, O.; Halcrow, M. A. Iron(II) Complexes of Tridentate Indazolylpyridine Ligands: Enhanced Spin-Crossover Hysteresis, and Ligand-Based Fluorescence. *Inorg. Chem.* **2015**, *54*, 682–693.

(12) Schäfer, B.; Bauer, T.; Faus, I.; Wolny, J. A.; Dahms, F.; Fuhr, O.; Lebedkin, S.; Wille, H.-C.; Schlage, K.; Chevalier, K.; Rupp, F.; Diller, R.; Schünemann, V.; Kappes, M. M.; Ruben, M. A Luminescent Pt_2Fe Spin Crossover Complex. *Dalton Trans.* **2017**, *46*, 2289–2302.

(13) (a) Hasegawa, Y.; Takahashi, K.; Kume, S.; Nishihara, H. Complete Solid State Photoisomerization of Bis(Dipyrazolylstyrylpyridine)Iron(II) to Change Magnetic Properties. *Chem. Commun.* **2011**, *47*, 6846–6848. (b) Takahashi, K.; Hasegawa, Y.; Sakamoto, R.; Nishikawa, M.; Kume, S.; Nishibori, E.; Nishihara, H. Solid-State Ligand-Driven Light-Induced

Spin Change at Ambient Temperatures in Bis(dipyrazolylstyrylpyridine)iron(II) Complexes. *Inorg. Chem.* **2012**, *51*, 5188−5198.

(14) (a) Abhervé, A.; Palacios-Corella, M.; Clemente-Juan, J. M.; Marx, R.; Neugebauer, P.; van Slageren, J.; Clemente-León, M.; Coronado, E. Bimetallic Mn^{III}–Fe^{II} Hybrid Complexes Formed by a Functionalized Mn^{III} Anderson Polyoxometalate Coordinated to Fe^{II}: Observation of a Field-Induced Slow Relaxation of Magnetization in the M^{III} Centres and a Photoinduced Spin-Crossover in the Fe^{II} Centres. *J. Mater. Chem. C* **2015**, *3*, 7936−7945. (b) Abhervé, A.; J. Recio-Carretero, M.; López-Jordà, M.; Clemente-Juan, J. M.; Canet-Ferrer, J.; Cantarero, A.; Clemente-León, M.; Coronado, E. Nonanuclear Spin-Crossover Complex Containing Iron(II) and Iron(III) Based on a 2,6-Bis(pyrazol-1-yl)pyridine Ligand Functionalized with a Carboxylate Group. *Inorg. Chem.* **2016**, *55*, 9361–9367.

(15) (a) Rajadurai, C.; Fuhr, O.; Kruk, R.; Ghafari, M.; Hahn, H.; Ruben, M. Above Room Temperature Spin Transition in a Metallo-Supramolecular Coordination Oligomer/Polymer. *Chem. Commun.* **2007**, 2636–2638. (b) Tovee, C. A.; Kilner, C. A.; Barrett, S. A.; Thomas, J. A.; Halcrow, M. A. A Back-to-Back Ligand with Dipyrazolylpyridine and Dipicolylamine Metal-Binding Domains. *Eur. J. Inorg. Chem.* **2010**, 1007–1012. (c) Kershaw Cook, L. J.; Fisher, J.; Harding, L. P.; Halcrow, M. A. An Iron(II) Spin-Crossover Metallacycle from a Back-to-Back Bis-[dipyrazolylpyridine]. *Dalton Trans.* **2015**, *44*, 9417–9425.

(16) (a) Devid, E. J.; Martinho, P. N.; Kamalakar, M. V.; Šalitroš, I.; Prendergast, Ú.; Dayen, J.-F.; Meded, V.; Lemma, T.; González-Prieto, R.; Evers, F.; Keyes, T. E.; Ruben, M.; Doudin, B.; van der Molen, S. J. Spin Transition in Arrays of Gold Nanoparticles and Spin Crossover Molecules. *ACS Nano* **2015**, *9*, 4496–4507. (b) Pukenas, L.; Benn, F.; Lovell, E.; Santoro, A.;

Kershaw Cook, L. J.; Halcrow, M. A.; Evans, S. D. Bead-Like Structures and Self-Assembled Monolayers from 2,6-Dipyrazolylpyridines and their Iron(II) Complexes. *J. Mater. Chem. C* **2015**, *3*, 7890–7896.

(17) Kumar, K. S.; Šalitroš, I.; Boubegtiten-Fezoua, Z.; Moldovan, S.; Hellwig, P.; Ruben, M. A Spin Crossover (SCO) Active Graphene-Iron(II) Complex Hybrid Material. *Dalton Trans.* **2018**, *47*, 35–40.

(18) (a) Secker, D.; Wagner, S.; Ballmann, S.; Härtle, R.; Thoss, M.; Weber, H. B. Resonant Vibrations, Peak Broadening, and Noise in Single Molecule Contacts: The Nature of the First Conductance Peak. *Phys. Rev. Lett.* **2011**, *106*, 136807/1–4. (b) Meded, V.; Bagrets, A.; Fink, K.; Chandrasekar, R.; Ruben, M.; Evers, F.; Bernand-Mantel, A.; Seldenthuis, J. S.; Beukman, A.; van der Zant, H. S. J. Electrical Control over the Fe(II) Spin Crossover in a Single Molecule: Theory and Experiment. *Phys. Rev. B* **2011**, *83*, 245415/1–13.

(19) Basak, S.; Hui, P.; Chandrasekar, R. Flexible and Optically Transparent Polymer Embedded Nano/Micro Scale Spin Crossover Fe(II) Complex Patterns/Arrays. *Chem. Mater.* **2013**, *25*, 3408−3413.

(20) (a) Gaspar, A. B.; Seredyuk, M. Spin Crossover in Soft Matter. *Coord. Chem. Rev.* **2014**, *268*, 41–58. (b) Kuroiwa, K. Supramolecular Control of Spin Crossover Phenomena Using Various Amphiphiles. *Inorganics* **2017**, *5*, 45/1–17.

(21) (a) Seredyuk, M.; Gaspar, A. B.; Ksenofontov, V.; Reiman, S.; Galyametdinov, Y.; Haase, W.; Rentschler, E.; Gütlich, P. Room Temperature Operational Thermochromic Liquid Crystals. *Chem. Mater.* **2006**, *18*, 2513–2519. (b) Seredyuk, M.; Gaspar, A. B.; Ksenofontov, V.; Galyametdinov, Y.; Verdaguer, M.; Villain, F.; Gütlich, P. One-Dimensional Iron(II)

Compounds Exhibiting Spin Crossover and Liquid Crystalline Properties in the Room Temperature Region. *Inorg. Chem.* **2008**, *47*, 10232–10245.

(22) Seredyuk, M.; Gaspar, A. B.; Ksenofontov, V.; Galyametdinov, Y.; Kusz, J.; Gütlich, P. Does the Solid-Liquid Crystal Phase Transition Provoke the Spin-State Change in Spin-Crossover Metallomesogens? *J. Am. Chem. Soc.* **2008**, *130*, 1431–1439.

(23) Seredyuk, M.; Gaspar, A. B.; Ksenofontov, V.; Galyametdinov, Y.; Kusz, J.; Gütlich, P. Iron(II) Metallomesogens Exhibiting Coupled Spin State and Liquid Crystal Phase Transitions near Room Temperature. *Adv. Funct. Mater.* **2008**, *18*, 2089–2101.

(24) Seredyuk, M.; Muñoz, M. C.; Ksenofontov, V.; Gütlich, P.; Galyametdinov, Y.; Real, J. A. Spin Crossover Star-Shaped Metallomesogens of Iron(II). *Inorg. Chem.* **2014**, *53*, 8442–8454.

(25) Abdullah, N.; Noor, N. L. M.; Nordin, A. R.; Halcrow, M. A.; MacFarlane, D. R.; Lazar, M. A.; Pringle, J. M.; Bruce, D. W.; Donnio, B.; Heinrich, B. Spin-Crossover, Mesomorphic and Thermoelectrical Properties of Cobalt(II) Complexes with Alkylated N_3-Schiff Bases. *J. Mater. Chem. C* **2015**, *3*, 2491–2499.

(26) Hayami, S.; Moriyama, R.; Shuto, A.; Maeda, Y.; Ohta, K.; Inoue, K. Spin Transition at the Mesophase Transition Temperature in a Cobalt(II) Compound with Branched Alkyl Chains. *Inorg. Chem.* **2007**, *46*, 7692–7694.

(27) Lee, Y. H.; Ohta, A.; Yamamoto, Y.; Komatsu, Y.; Kato, K.; Shimizu, T.; Shinoda, H.; Hayami, S. Iron(II) Spin Crossover Complexes with Branched Long Alkyl Chain. *Polyhedron* **2011**, *30*, 3001–3005.

(28) (a) Fujigaya, T.; Jiang, D.-L.; Aida, T. Switching of Spin States Triggered by a Phase Transition: Spin-Crossover Properties of Self-Assembled Iron(II) Complexes with Alkyl-Tethered Triazole Ligands. *J. Am. Chem. Soc.* **2003**, *125*, 14690–14691. (b) Romero-Morcillo, T.; Seredyuk, M.; Muñoz, M. C.; Real, J. A. Meltable Spin Transition Molecular Materials with Tunable *T*c and Hysteresis Loop Width *Angew. Chem. Int. Ed.* **2015**, *54*, 14777–14781.

(29) Halcrow, M. A. Structure:Function Relationships in Molecular Spin-Crossover Complexes. *Chem. Soc. Rev.* **2011**, *40*, 4119–4142.

(30) Zhang, W.; Zhao, F.; Liu, T.; Yuan, M.; Wang, Z.-M.; Gao, S. Spin Crossover in a Series of Iron(II) Complexes of 2-(2-Alkyl-2*H*-tetrazol-5-yl)-1,10-phenanthroline: Effects of Alkyl Side Chain, Solvent, and Anion. *Inorg. Chem.* **2007**, *46*, 2541–2555.

(31) See *eg* (a) Nielsen, P.; Toftlund, H.; Bond, A. D.; Boas, J. F.; Pilbrow, J. R.; Hanson, G. R.; Noble, C.; Riley, M. J.; Neville, S. M.; Moubaraki, B.; Murray, K. S. Systematic Study of Spin Crossover and Structure in $[Co(terpyRX)_2](Y)_2$ Systems (terpyRX = 4'-alkoxy-2,2':6',2''-terpyridine, X = 4, 8, 12, Y = BF_4^-, ClO_4^-, PF_6^-, BPh_4^-). *Inorg. Chem.* **2009**, *48*, 7033–7047. (b) Martinho, P. N.; Harding, C. J.; Müller-Bunz, H.; Albrecht, M.; Morgan, G. G. Inducing Spin Crossover in Amphiphilic Iron(III) Complexes. *Eur. J. Inorg. Chem.* **2010**, 675–679. (c) Kitchen, J. A.; White, N. G.; Gandolfi, C.; Albrecht, M.; Jameson, G. N. L.; Tallon, J. L.; Brooker, S. Room-Temperature Spin Crossover and Langmuir–Blodgett Film Formation of an Iron(II) Triazole Complex Featuring a Long Alkyl Chain Substituent: the Tail that Wags the Dog. *Chem. Commun.* **2010**, *46*, 6464–6466. (d) Scott, H. S.; Moubaraki, B.; Paradis, N.; Chastanet, G.; Létard, J.-F.; Batten, S. R.; Murray, K. S. 2,2'-Dipyridylamino-Based Ligands with Substituted

Alkyl Chain Groups and their Mononuclear-M(II) Spin Crossover Complexes. *J. Mater. Chem. C* **2015**, *3*, 7845–7857.

(32) (a) Galyametdinov, Y.; Ksenofontov, V.; Prosvirin, A.; Ovchinnikov, I.; Ivanova, G.; Gütlich, P.; Haase, W. First Example of Coexistence of Thermal Spin Transition and Liquid-Crystal Properties. *Angew. Chem. Int. Ed.* **2001**, *40*, 4269–4271. (b) Hayami, S.; Motokawa, N.; Shuto, A.; Masuhara, N.; Someya, T.; Ogawa, Y.; Inoue, K.; Maeda, Y. Photoinduced Spin Transition for Iron(II) Compounds with Liquid-Crystal Properties. *Inorg. Chem.* **2007**, *46*, 1789–1794.

(33) Oso, Y.; Ishida, T. Spin-crossover Transition in a Mesophase Iron(II) Thiocyanate Complex Chelated with 4-Hexadecyl-*N*-(2-pyridylmethylene)aniline *Chem. Lett.* **2009**, *38*, 604–605.

(34) (a) Schlamp, S.; Weber, B.; Naik, A. D.; Garcia, Y. Cooperative Spin Transition in a Lipid Layer Like System. *Chem. Commun.* **2011**, *47*, 7152–7154. (b) Rosario-Amorin, D.; Dechambenoit, P.; Bentaleb, A.; Rouzières, M.; Mathonière, C.; Clérac, R. Multistability at Room Temperature in a Bent-Shaped Spin-Crossover Complex Decorated with Long Alkyl Chains. *J. Am. Chem. Soc.* **2018**, *140*, 98–101.

(35) (a) Hayami, S.; Shigeyoshi, Y.; Akita, M.; Inoue, K.; Kato, K.; Osaka, K.; Takata, M.; Kawajiri, R.; Mitani, T.; Maeda, Y. Reverse Spin Transition Triggered by a Structural Phase Transition. *Angew. Chem. Int. Ed.* **2005**, *44*, 4899–4903. (b) Hayami, S.; Murata, K.; Urakami, D.; Kojima, Y.; Akita, M.; Inoue, K. Dynamic Structural Conversion in a Spin-Crossover Cobalt(II) Compound with Long Alkyl Chains. *Chem. Commun.* **2008**, 6510–6512. (c) Hayami, S.; Kato, K.; Komatsu, Y.; Fuyuhiro, A.; Ohba, M. Unique Spin Transition and Wide Thermal

Hysteresis Loop for a Cobalt(II) Compound with Long Alkyl Chain. *Dalton Trans.* **2011**, *40*, 2167–2169. (d) Ohtani, R.; Egawa, S.; Nakaya, M.; Ohmagari, H.; Nakamura, M.; Lindoy, L. F.; Hayami, S. Metal Dilution Effects on the Reverse Spin Transition in Mixed Crystals of Type $[Co_{1-x}Zn_x(C_{16}\text{-terpy})_2](BF_4)_2$ (x = 0.1−0.7). *Inorg. Chem.* **2016**, *55*, 3332–3337.

(36) Ostermeier, M.; Berlin, M.-A.; Meudtner, R. M.; Demeshko, S.; Meyer, F.; Limberg, C.; Hecht, S. Complexes of Click-Derived Bistriazolylpyridines: Remarkable Electronic Influence of Remote Substituents on Thermodynamic Stability as well as Electronic and Magnetic Properties. *Chem. Eur. J.* **2010**, *16*, 10202–10213.

(37) Vermonden, T.; Branowska, D.; Marcelis, A. T. M.; Sudhölter, E. J. R. Synthesis of 4-Functionalized Terdendate Pyridine-Based Ligands. *Tetrahedron* **2003**, *59*, 5039–5045.

(38) Sheldrick, G. M. Crystal Structure Refinement with *SHELXL*. *Acta Cryst. Sect. C.: Struct. Chem.* **2015**, *71*, 3–8.

(39) Barbour, L. J. *X-Seed* – A Software Tool for Supramolecular Crystallography. *J. Supramol. Chem.* **2001**, *1*, 189−191.

(40) O'Connor, C. J. Magnetochemistry – Advances in Theory and Experimentation. *Prog. Inorg. Chem.* **1982**, *29*, 203–283.

(41) (a) Evans, D. F. The Determination of the Paramagnetic Susceptibility of Substances in Solution by Nuclear Magnetic Resonance. *J. Chem. Soc.* **1959**, 2003–2005. (b) Schubert, E. M. Utilizing the Evans Method with a Superconducting NMR Spectrometer in the Undergraduate Laboratory. *J. Chem. Educ.* **1992**, *69*, 62.

(42) García, B.; Ortega, J. C. Excess Viscosity η^{E}, Excess Volume V^{E}, and Excess Free Energy of Activation ΔG^{*E} at 283, 293, 303, 313, and 323 K for Mixtures of Acetonitrile and Alkyl Benzoates. *J. Chem. Eng. Data* **1988**, *33*, 200–204.

(43) Equation 1 is a rearrangement of $\Delta G = -RT\ln K$, where K is the ratio of high-spin and low-spin molecules in the sample at temperature T; and, $\Delta G = \Delta H - T\Delta S$. Equation 2 reflects that, at $T_{½}$, the SCO is at equilibrium so $\Delta G = 0$ and $\Delta H = T_{½}\Delta S$.

(44) Kaszynski, P.; Januszko, A.; Ohta, K.; Nagamine, T.; Potaczek, P.; Young, V. G. jr.; Endo, Y. Conformational Effects on Mesophase Stability: Numerical Comparison of Carborane Diester Homologous Series with their Bicyclo[2.2.2]Octane, Cyclohexane and Benzene Analogues. *Liq. Cryst.* **2008**, *35*, 1169–1190.

(45) While the L^3C_m complex structures with m = 6 and 16 are isostructural with the powder samples of those compounds, crystals of $[Fe(L^3C_{14})_2][BF_4]_2\cdot 2MeCN$ were obtained from a different solvent and are different from the powder samples by powder diffraction (Figure S41).

(46) See *eg* (a) Sugiyarto, K. H.; Weitzner, K.; Craig, D. C.; Goodwin, H. A. Structural, Magnetic and Mössbauer Studies of Bis(2,6-bis(pyrazol-3-yl)pyridine)iron(II) Triflate and its Hydrates. *Aust. J. Chem.* **1997**, *50*, 869–873. (b) Roubeau, O.; Haasnoot, J. G.; Codjovi, E.; Varret, F.; Reedijk, J. Spin Transition Regime in New One-Dimensional Polymeric Iron(II) Compounds. Importance of the Water Content for the Thermal and Optical Properties. *Chem. Mater.* **2002**, *14*, 2559–2566. (c) Clemente-León, M.; Coronado, E.; Giménez-López, M. C.; Romero, F. M.; Asthana, S.; Desplanches, C.; Létard, J.-F. Structural, Thermal and Photomagnetic Properties of Spin Crossover $[Fe(bpp)_2]^{2+}$ Salts Bearing $[Cr(L)(ox)_2]^{-}$ Anions. *Dalton Trans.* **2009**, 8087–8095. (d) Bushuev, M. B.; Daletsky, V. A.; Pishchur, D. P.; Gatilov,

Y. V.; Korolkov, I. V.; Nikolaenkova, E. B.; Krivopalov, V. P. Unprecedented Bistability Domain and Interplay Between Spin Crossover and Polymorphism in a Mononuclear Iron(II) Complex. *Dalton Trans.* **2014**, *43*, 3906–3910.

(47) (a) Abhervé, A.; Clemente-León, M.; Coronado, E.; Gómez-García, C. J.; López-Jordà, M. A. Spin-Crossover Complex Based on a 2,6-Bis(pyrazol-1-yl)pyridine (1-bpp) Ligand Functionalized with a Carboxylate Group. *Dalton Trans.* **2014**, *43*, 9406–9409. (b) Bridonneau, N.; Rigamonti, L.; Poneti, G.; Pinkowicz, D.; Forni, A.; Cornia, A. Evidence of Crystal Packing Effects in Stabilizing High or Low Spin States of Iron(II) Complexes with Functionalized 2,6-Bis(pyrazol-1-yl)pyridine Ligands. *Dalton Trans.* **2017**, *46*, 4075–4085.

(48) See *eg* (a) Reeder, K. A.; Dose, E. V.; Wilson, L. J. Solution-State Spin-Equilibrium Properties of the Tris[2-(2-pyridyl)imidazole]iron(II) and Tris[2-(2-pyridyl)benzimidazole]iron(II) Cations. *Inorg. Chem.* **1978**, *17*, 1071–1075. (b) Chum, H. L.; Vanin, J. A.; Holanda, M. I. D. Tris(2-(aminomethyl)pyridine)iron(II): a New Spin-State Equilibrium in Solution. *Inorg. Chem.* **1982**, *21*, 1146–1152. (c) Turner, J. W.; Schultz, F. A. Solution Characterization of the Iron(II) Bis(1,4,7-Triazacyclononane) Spin-Equilibrium Reaction. *Inorg. Chem.* **2001**, *40*, 5296–5298. (d) Barrett, S. A.; Kilner, C. A.; Halcrow, M. A. Spin-Crossover in $[Fe(3\text{-bpp})_2][BF_4]_2$ in Different Solvents – a Dramatic Stabilisation of the Low-Spin State in Water. *Dalton Trans.* **2011**, *40*, 12021–12024. (e) Creutz, S. E.; Peters, J. C. Spin-State Tuning at Pseudo-tetrahedral d^6 Ions: Spin Crossover in $[BP_3]Fe^{II}–X$ Complexes. *Inorg. Chem.* **2016**, *55*, 3894–3906. (f) Rodríguez-Jiménez, S.; Brooker, S. Solid Versus Solution Spin Crossover and the Importance of the Fe−N≡C(X) Angle. *Inorg. Chem.* **2017**, *56*, 13697–13708.

(49) Gütlich, P.; Hauser, A.; Spiering, H. Thermal and Optical Switching of Iron(II) Complexes. *Angew. Chem. Int. Ed.* **1994**, *33*, 2024–2054.

(50) McKenna, G. B.; Simon, S. L. Challenges in the Dynamics and Kinetics of Glass-Forming Polymers. *Macromolecules* **2017**, *50*, 6333–6361

(51) Holland, J. M.; McAllister, J. A.; Kilner, C. A.; Thornton-Pett, M.; Bridgeman, A. J.; Halcrow, M. A. Stereochemical Effects on the Spin-State Transition Shown by Salts of $[FeL_2]^{2+}$ [L = 2,6-Di(pyrazol-1-yl)pyridine]. *J. Chem. Soc. Dalton Trans.* **2002**, 548–554.

(52) (a) Bodenthin, Y.; Schwarz, G.; Tomkowicz, Z.; Geue, T.; Haase, W.; Pietsch, U.; Kurth, D. G. Liquid Crystalline Phase Transition Induces Spin Crossover in a Polyelectrolyte Amphiphile Complex. *J. Am. Chem. Soc.* **2009**, *131*, 2934–2941. (b) Schwarz, G.; Bodenthin, Y.; Tomkowicz, Z.; Haase, W.; Geue, T.; Kohlbrecher, J.; Pietsch, U.; Kurth, D. G. Tuning the Structure and the Magnetic Properties of Metallo-Supramolecular Polyelectrolyte-Amphiphile Complexes. *J. Am. Chem. Soc.* **2011**, *133*, 547–558.